ACS Sustainable Chemistry & Engineering

pubs.acs.org/journal/ascecg

Research Article

Phase- and Crystallinity-Tailorable MnO_2 as an Electrode for Highly Efficient Hybrid Capacitive Deionization (HCDI)

Jie Jin, Man Li, Mengting Tang, Yang Li,* Yangyang Liu, Hui Cao, and Feihu Li*

Cite This: *ACS Sustainable Chem. Eng.* 2020, 8, 11424−11434

Read Online

ACCESS | Metrics & More | Article Recommendations | Supporting Information

ABSTRACT: Hybrid capacitive deionization (HCDI) is an emerging and promising technology for water desalination and has been extensively explored in recent years. Designing a structure-tailorable electrode material has been proved to be a valid strategy for achieving a higher salt adsorption capacity (SAC). In this study, MnO_2 materials with tailorable phase compositions and crystallinities were prepared hydrothermally and then evaluated as electrodes for removal of ions from a NaCl solution in a membrane-free HCDI cell. MnO_2 electrode materials tested in the HCDI system include poorly crystalline δ-MnO_2 along with abundant amorphous phases (MnO_2-1h); crystalline δ-MnO_2 with plentiful amorphous MnO_2 (MnO_2-2h); MnO_2 mixtures of α-, δ-, and amorphous MnO_2 (MnO_2-5h); and α-MnO_2 nanowires with minor amorphous MnO_2 (MnO_2-12h). Our results revealed that the phase composition and the crystallinity of MnO_2 materials govern their specific capacitances and thus the SAC values. When the cell voltage is 1.2 V, the lamellar-structured poorly crystalline MnO_2-1h electrode with the lowest crystallinity demonstrates the highest SACs of 13.84 mg g^{-1} in 100 mg L^{-1} NaCl (1.71 mM) and 21.32 mg g^{-1} in 500 mg L^{-1} NaCl (8.56 mM) solutions, respectively. The desalination efficiencies of the MnO_2−1h electrode are remarkable and much greater than other MnO_2-based electrodes under similar conditions (e.g., NaCl concentrations, cell voltage, etc.). This study sheds light on the significance of understanding the fundamentals of both the phase composition and crystallinity in defining the desalination performance of MnO_2 electrodes.

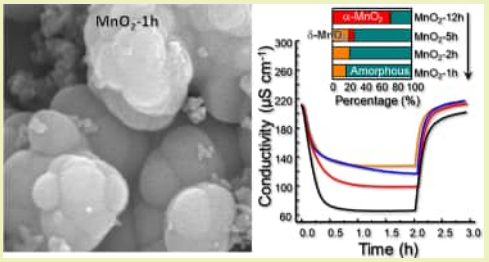

KEYWORDS: *MnO_2, hybrid capacitive deionization (HCDI), desalination, phase transition, membrane-free*

INTRODUCTION

One of the serious global problems at present and especially in the future is the shortage of fresh water that has been attracting worldwide attention. Two-thirds of the global population will face the conditions in which available clean water does not meet the demand by 2025.[1] On the other hand, the sea and ocean account for 96.5% of total water resources and are promising to be used as fresh water resources with novel desalination technologies.[2−4] One of the most robust and cost-effective technologies for desalination of water is capacitive deionization (CDI), which has been developed as an emerging ion removal approach over the past two decades and drawn extensive attention in recent years.[4−10]

Generally, a typical CDI desalination is the process in which saline water flows between two electrodes under a specific stable voltage, allowing the directional migrations of ions between the planar electrodes.[11] Both cations and anions are electrosorbed and accumulated on the oppositely charged electrodes constantly. Once the electrosorption reaches saturation, the ions are released from the electrodes into the solution and hence the electrodes are regenerated by applying a reverse potential.[4] The salt adsorption capacity (SAC) of the electrode materials plays a crucial role in the desalination efficiency of a single CDI cell and thus the commercial realization of CDI technology.[4] Traditionally, carbon materials with high surface areas, including activated carbon (AC),[12,13] graphene,[9,10,14] carbon nanotube,[15] and biochar,[16] were extensively employed as the electrodes for CDI. The salt ions (i.e., Na^+ and Cl^-) are electrosorbed in the electric double layer on the surface of the carbon electrodes and then stored inside the pores of the carbon electrodes. However, carbon electrodes are often limited in their SACs by both the available surface areas and pore structures.[6,8,17] It has been shown that the sub-nanometers pores (<1 nm) rather than the total pore volume are responsible for the SAC of carbide-derived carbon (CDC) electrodes.[18] Nevertheless, the SAC limitation of carbon electrodes can be overcome by the replacement of carbon electrodes with faradaic electrodes that react with the ions in solution to proceed with the faradic reactions. Based on this concept, a desalination battery system with two faradaic electrodes and a hybrid capacitive deionization (HCDI) system combining one faradaic electrode with one carbon electrode have been invented.[19,20] Both systems have shown

Received: June 3, 2020
Revised: June 28, 2020
Published: July 8, 2020

enhanced SAC over the conventional CDI systems solely using carbon electrodes, but HCDI has higher ion adsorption rates compared to the desalination battery system.[8,20] Of various faradaic electrode materials, MnO_2 has been demonstrated as one of the most attractive electrode materials for water desalination due to its tailorable crystal structure, low cost, low aquatic toxicity, high stability in aqueous environments, high electrochemical activity, and high theoretical specific capacity (1370 F g^{-1}).[7,8,20−28] Several attempts have been reported to evaluate the saline desalination performance with MnO_2-based electrode materials, which has also been highlighted by a recent review paper.[29] Zou et al. reported for the first time the application of α-MnO_2/nanoporous carbon (NC) composites as electrodes in CDI and found that a SAC of 0.987 mg g^{-1} was achieved for desalination of 50 mL of NaCl (35 mg L^{-1}).[30] Inspired by this pioneering study, other investigators have developed a variety of manganese oxides/carbon hybrid electrodes such as AC@α-MnO_2,[22] PCS@δ-MnO_2,[31] MWCNTs@δ-MnO_2,[32] OMC@MnO_x,[33] graphene@α-MnO_2,[24] and ECNF@MnO_x,[34] of which their SACs did not exceed 10 mg g^{-1} in CDI systems (note: PCS, porous carbon sphere; MWCNTs, multiwalled carbon nanotubes; OMC, ordered mesoporous carbon; ECNF, electrospun carbon nanofiber). Using hollow carbon@δ-MnO_2 as the cathode and positive-charged hollow carbon sphere (PHC) as the anode in a membrane-free HCDI system, Qiu et al. found that a SAC as high as 19.6 mg g^{-1} was obtained in 100 mg L^{-1} NaCl.[28] Shi et al. coated thin films of MnO_x onto vertically aligned carbon nanotubes (VACNTs) using atomic layer deposition and fabricated VACNT@MnO_x electrodes, which exhibited a remarkable sodium ion adsorption capacity of 490 ± 30 μmol of sodium per gram material.[35] More recently, Bharath et al. reported a hybrid electrode of Mn_3O_4 nanowires immobilized on reduced graphene oxide (RGO@Mn_3O_4), which displayed a high SAC of 34.2 mg g^{-1} at 1.2 V in 1000 mg L^{-1} NaCl solution.[36] In addition to these hybridization approaches, other strategies such as electrode reversing, crystal structure tailoring, and morphologic altering of MnO_2 materials were also reported.[7,8,23] Using δ-MnO_2 as the anode rather than the cathode in an HCDI cell, Qiu et al. reported an interesting finding that a SAC up to 14.9 mg g^{-1} was achieved in 500 mg L^{-1} NaCl and that the cell was highly stable with a SAC retention ratio of 90.5% over 350 cycles.[7] Pomerantseva et al. compared the desalination performance of a set of MnO_2 nanowires (NWs) in HCDI cells with ion-exchange membranes and found that the SACs are as high as 22.1, 23.3, 27.8, and 27.3 mg g^{-1} for α-MnO_2, Tod-MnO_2, 2×n-MnO_2, and hybrid MnO_2 nanowire electrodes, respectively (note that the feed solution is 876.6 mg L^{-1} NaCl).[8] Yang and co-workers investigated the desalination properties of one-dimensional (1D) hollandite α-MnO_2, two-dimensional (2D) birnessite δ-MnO_2, and three-dimensional (3D) spinel λ-MnO_2 in membrane-free HCDI cells and observed that poorly crystalline forms of α-MnO_2 and δ-MnO_2 exhibited the highest SACs of 9.93 and 9.35 mg g^{-1}, respectively.[23] MnO_2 exists in a wide variety of polymorphs with different tunnel structures, morphologies, and electrical conductivities, all of which determine its ion storage ability.[37,38] Note that the hydrothermally synthesized MnO_2 without the addition of specific directing agents is a mixture of several crystal phases.[8,23,39] Until now, a few studies have evaluated the desalination properties of such MnO_2 mixtures with two or more crystalline structures (phase components) in CDI systems.[8] Furthermore, an earlier study indicated that capture of cations in MnO_2-based cathodes most likely occurred in two different manners—intercalation of cations by crystalline MnO_2 and surface adsorption by amorphous MnO_2,[40] but the influences of phase composition and crystallinity of MnO_2 on their desalination performance have not been elucidated yet.

In this work, the effects of phase composition and crystallinity of MnO_2 on the desalination performance were considered for the first time. A set of MnO_2 with varying phase compositions, crystallinities, and morphologies were prepared: poorly crystalline δ-MnO_2 with abundant amorphous MnO_2 (MnO_2-1h), crystalline δ-MnO_2 with plentiful amorphous MnO_2 (MnO_2-2h), MnO_2 mixtures with various crystal phases (MnO_2-5h), and 1D α-MnO_2 nanowires with minor amorphous MnO_2 (MnO_2-12h). The desalination performances of these MnO_2 electrodes were evaluated in terms of SAC using a membrane-free HCDI system. The relationship between the phase composition, crystallinity, and desalination performance has also been explored for the optimal design of MnO_2 electrode materials for CDI applications.

MATERIALS AND METHODS

Preparation of MnO_2 Electrode Materials. The one-pot hydrothermal synthesis method was used for the preparation of MnO_2 electrode materials, as depicted in Scheme 1. Briefly, 0.5 g of

Scheme 1. Schematic Illustration of the Formation Process of MnO_2 via a Hydrothermal Reaction[a]

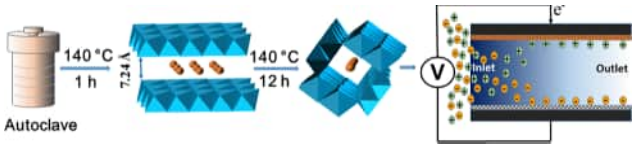

[a]The orange balls refer to K^+ ions in the MnO_6 octahedral interlayers or tunnels.

$KMnO_4$ (AR grade, Lingfen Chemical Co., Shanghai, China) and 0.2 g of $MnSO_4{\cdot}H_2O$ (98.0%, Aladdin Chemical Co., Shanghai, China) were used as the manganese precursors and mixed in 50 mL of deionized water. After stirring for 30 min, the mixture was transferred into a 100 mL Teflon-lined stainless steel autoclave and heated at 140 °C for different durations (i.e., 1, 2, 5, and 12 h). Then, the autoclave was cooled down to room temperature. After centrifugation, the as-prepared MnO_2 materials were collected and washed with excess deionized water until the conductivity of the supernatant is below 10 μS cm^{-1}. The resultant MnO_2 precipitates were collected and dried at 60 °C in the vacuum oven for 12 h.

Material Characterizations. X-ray diffraction (XRD) analysis was conducted on an XRD-6100 diffractometer (Shimadzu, Japan) at a tube voltage of 40 kV and a tube current of 30 mA with Cu Kα radiation. Weight percentages of mineral phases in the as-prepared MnO_2 samples were obtained using the whole-pattern fitting (WPF) and Rietveld refinement method embedded in Jade software (MDI, California). The crystallinity values of the as-prepared MnO_2 samples were calculated by Jade software. Scanning electron microscopy (SEM) was performed using a Hitachi SU1510 microscope at an accelerating voltage of 1.5 kV. The Brunauer−Emmett−Teller (BET) specific surface areas and the Barrett−Joyner−Halenda (BJH) pore size distributions of the MnO_2 samples were measured by nitrogen absorption−desorption at −196 °C using a Quantachrome gas absorption analyzer (iQ-AG-MP). XPS data were obtained with an electron spectrometer (UIVAC-PHI, Japan) using 300 W Al Kα radiation. The pressure in the analysis chamber was maintained below 3×10^{-9} mbar. The XPS photoelectron binding energies (BEs) of the

https://dx.doi.org/10.1021/acssuschemeng.0c04101
ACS Sustainable Chem. Eng. 2020, 8, 11424−11434

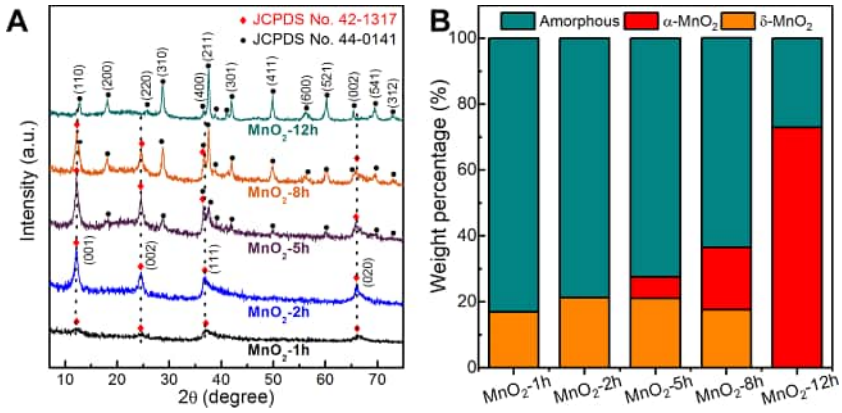

Figure 1. (A) XRD patterns of as-prepared MnO_2 samples and (B) mineral phase percentage of the as-prepared MnO_2 samples as calculated by Rietveld refinement.

adventitious carbon species, i.e., the C 1s line at 284.6 eV, were used to correct the observed binding energies for surface charging.

Electrochemical Measurements. The cyclic voltammetry (CV), galvanostatic charge−discharge (GCD), and electrochemical impedance spectroscopy (EIS) were measured in 1 M NaCl solution on a CHI 660D electrochemical workstation (CH Instruments Inc., Shanghai, China). The three-electrode system consists of a MnO_2 electrode (working electrode), a platinum wire/foil electrode (counter electrode), and a Ag/AgCl (3 M KCl) electrode (reference electrode). The MnO_2 electrode was fabricated by coating a mixture of 85 wt % MnO_2 material, 10 wt % acetylene black (Alfa Aesar, Shanghai, China), and 5 wt % poly(tetrafluoroethene) (PTFE, Aladdin Chemical Co.) onto a graphite plate with a size of 1 cm × 2 cm. Specific capacitances of the MnO_2 electrodes were determined from GCD curves by following a standard method.[41]

Capacitive Deionization Experiments. The preparation of CDI electrodes was the same as the above procedure for the electrochemical measurements using the graphite plate as the current collectors. The active capacitive deionization area was set up to a size of 5 cm × 5 cm. The electrode materials of the cathode and anode were MnO_2 and activated carbon (JCNANO Technology Co., Nanjing, China), respectively. The total mass of exposed materials was 100 mg for each electrode, and the average thickness of the electrodes was about 100 μm after roll-press. Before the CDI test, dissolved oxygen (DO) in the NaCl solution was expelled with nitrogen for 10 min to avoid side reactions. A total volume of 40 mL of NaCl solution was continuously circulated within a homemade CDI cell (Figure S1, Supporting Information) through a BT-100 peristaltic pump (Longer Precision Pump Co., China) at a flow rate of 40 mL min^{-1}. The effluent conductivity at a constant cell voltage of 0 V was recorded as the baseline. The desalination experiments were conducted at a constant cell voltage of 1.2 V with a starting NaCl concentration ranging from 50 to 500 mg L^{-1} (0.86−8.56 mM). The salt concentration change was measured by monitoring the effluent conductivity with a DDSJ-308A conductivity meter (INESA Scientific Instrument Co., Shanghai, China). After the effluent conductivity decreased to a constant, the electrodes were then regenerated by applying a short-circuit until the effluent conductivity was restored. Each experiment was cycled three times before the results were recorded. Values from the last cycle were used to compute the SAC (mg g^{-1}) according to eq 1

$$\mathrm{SAC} = \frac{(C_0 - C_e)V}{m} \tag{1}$$

where C_0 (mg g^{-1}) and C_e (mg g^{-1}) refer to the initial and equilibrium concentrations of the NaCl solution, respectively, V (mL) is the volume of the NaCl solution, and m (g) is the total mass of the active materials in both the anode and the cathode.

The charge efficiency (Λ) was used as another metric for evaluation of the CDI performance,

$$\Lambda = \frac{\mathrm{SAC} \times F}{\sum} \tag{2}$$

where F is the Faraday constant (96 485 C mol^{-1}) and $\sum$ is the total charge associated with the integrated corresponding current (C g^{-1}).

The Kim−Yoon plot was also employed to evaluate the CDI performance.[42] The salt adsorption capacity at a certain time (SAC_t, mg g^{-1}) and the corresponding salt adsorption rate (SAR_t, mg g^{-1} min^{-1}) can be calculated by eqs 3 and 4

$$\mathrm{SAC}_t = \frac{(C_0 - C_t)V}{m} \tag{3}$$

$$\mathrm{SAR}_t = \frac{\mathrm{SAC}_t}{t} \tag{4}$$

where C_t (mg L^{-1}) is the instantaneous concentration of NaCl at time t (min).

RESULTS AND DISCUSSION

Physicochemical Characteristics of As-Prepared MnO_2. Figure 1A shows the XRD patterns of the as-prepared MnO_2 samples with different hydrothermal reaction times at 140 °C. After a hydrothermal reaction at 140 °C for 1 h, the XRD profile of sample MnO_2-1h features several strong and broad diffuse reflections along with four weak reflections at 2θ = 12.2, 24.5, 37.0, and 66.0°, which can be easily indexed to the (001), (002), (111), and (020) planes of the poorly crystalline δ-MnO_2 (JCPDS No. 44-1317), respectively.[43] This observation indicates that MnO_2-1h is primarily composed of amorphous manganese oxide with tiny poorly crystalline δ-MnO_2. As the reaction time increased to 2 h, the intensities of the above four reflections increased apparently without any changes in the 2θ position, implying that the phase transition of amorphous MnO_2 to poorly crystalline δ-MnO_2 and further to crystalline δ-MnO_2 had occurred. The four well-defined peaks can be assigned to the lamellar-structured reflections of δ-MnO_2.[44] The basal spacing of MnO_2-2h is 7.24 Å, as calculated by the Bragg equation. No reflections were observed in the profile of MnO_2-2h, suggesting that other MnO_2 phases have not yet formed after a hydrothermal reaction for 2 h. Further prolonging the reaction time to 5 h led to a clear increase in the crystallinity of δ-MnO_2 and the emergence of several new reflections at 2θ = 18.2, 28.7, 37.6, 38.9, 41.9, 49.9, and 60.1°, which can be readily assigned to poorly crystalline α-MnO_2 phase (JCPDS No. 44-0141).[8,23] This indicates that a part of lamellar-structured δ-MnO_2 has transited into tunnel-structured α-MnO_2 due to the rearrangements of MnO_6

https://dx.doi.org/10.1021/acssuschemeng.0c04101
ACS Sustainable Chem. Eng. 2020, 8, 11424−11434

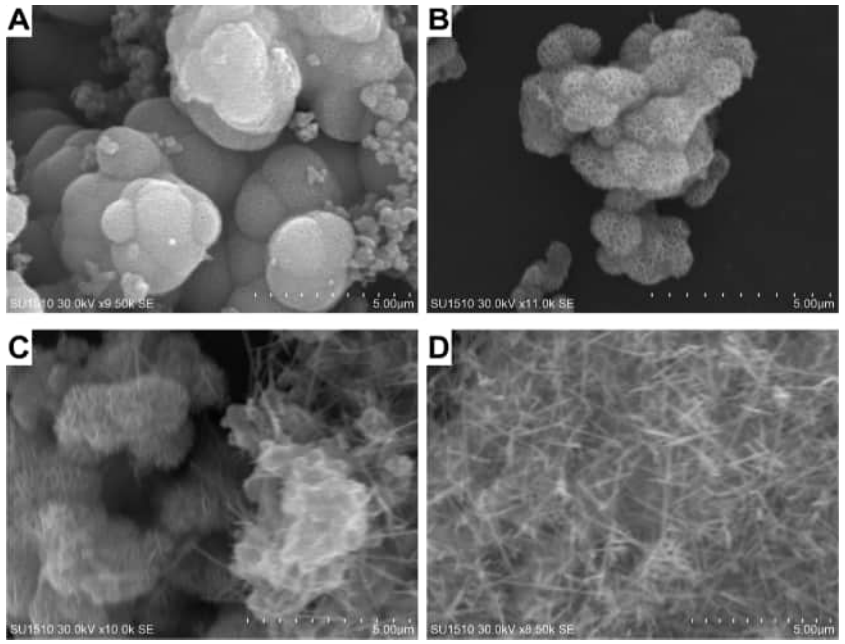

Figure 2. SEM images of (A) MnO_2-1h, (B) MnO_2-2h, (C) MnO_2-5h, and (D) MnO_2-12h.

Figure 3. Proposed morphological and phase evolution of the as-prepared MnO_2 with incubation time.

octahedral units under the autogenous pressure. The δ-to-α phase transition proceeded evidently with the increasing reaction time to 8 h and was almost done until 12 h, as validated by the XRD profile of MnO_2-12h, in which the reflections of δ-MnO_2 disappeared completely and only well-defined reflections of α-MnO_2 could be observed (Figure 1A). This δ-to-α phase transition has also been observed early for MnO_2 under hydrothermal conditions.[45,46]

Whole-pattern fitting (WPF) and Rietveld refinement were used to semiquantitatively calculate the approximate weight percentages of amorphous, δ, and α phases in different MnO_2 samples. The fitting results are shown in Figure 1B and Table S1 (Supporting Information). Note that all of the WPF errors are below 15%, implying that good fitting results are obtained. As the reaction time increased from 1 to 12 h, the weight percentage of amorphous phase decreased gradually from 83.0 wt % in MnO_2-1h to 27.1 wt % in MnO_2-12h, while the α-MnO_2 percentage remained at zero in the first 2 h and then increased evidently from 6.4 wt % in MnO_2-5h to 72.9 wt % in MnO_2-12h. The δ-MnO_2 percentage increased slightly until reaching a maximum of 22.1 wt % after a reaction of 5 h and then dropped to zero after 12 h. The phase transition can, therefore, be described as follows: (i) only amorphous-to-δ phase transition occurred in the first 3 h probably; (ii) the δ-to-α phase transition was likely to launch after a reaction of 4 h along with the continuous amorphous-to-δ phase transition in the period of 3−8 h; (iii) the amorphous to δ and further to α phase transition proceeded until δ-MnO_2 was exhausted after 12 h of reaction.

The morphological evolution of the as-prepared MnO_2 samples (i.e., MnO_2-1h, MnO_2-2h, MnO_2-5h, and MnO_2-12h) is depicted by SEM in Figure 2. Amorphous MnO_2 particles (MnO_2-1h) show the morphology of spheroidal aggregates with plenty of shallow pits on the surface along with a variety of smaller particles around (Figure 2A). Note that the smaller particles disappeared and the semispherical aggregates adhered together to form a larger pinecone-like aggregation during the hydrothermal reaction from 1 to 2 h, indicating that

https://dx.doi.org/10.1021/acssuschemeng.0c04101
ACS Sustainable Chem. Eng. 2020, 8, 11424−11434

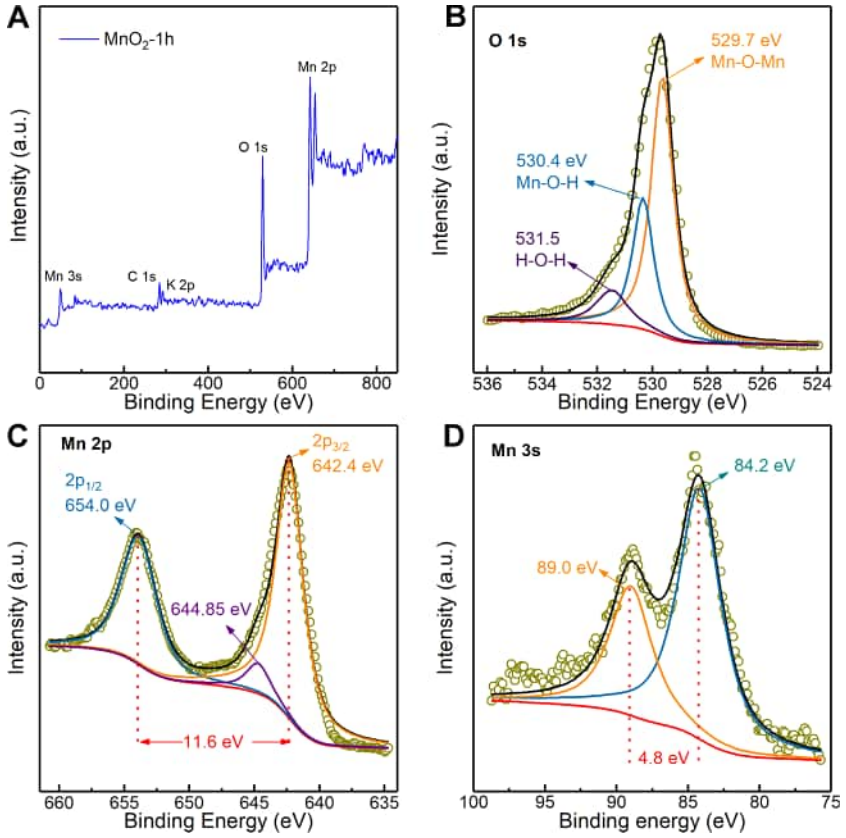

Figure 4. XPS spectra of MnO_2-1h. (A) Survey spectrum and fine spectrum of (B) O 1s, (C) Mn 2p, and (D) Mn 3s.

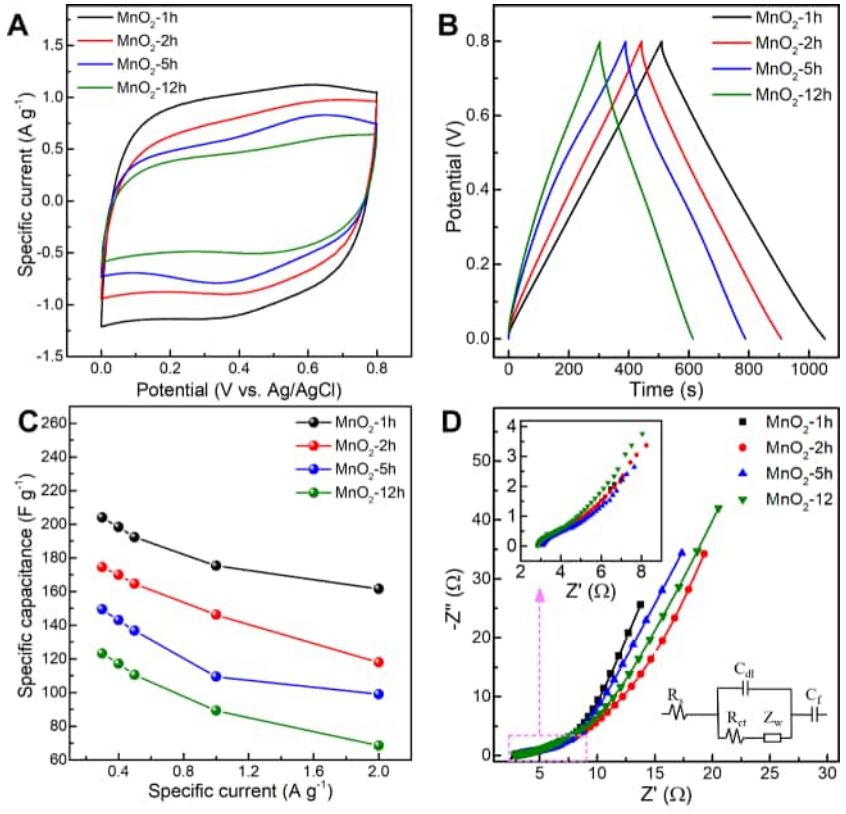

Figure 5. (A) CV curves of MnO_2 electrodes at 5 mV s^{-1} in 1 M NaCl solution, (B) GCD curves of MnO_2 electrodes at 0.3 A g^{-1} in 1 M NaCl solution, (C) specific capacitances of MnO_2 electrodes under different charge−discharge currents, and (D) Nyquist plots of EIS and the fitting curves; the inset shows the equivalent electric circuit.

https://dx.doi.org/10.1021/acssuschemeng.0c04101
ACS Sustainable Chem. Eng. 2020, 8, 11424−11434

Ostwald ripening had occurred. After 12 h of the hydrothermal reaction, the semispherical aggregates transformed to nanowires probably via a dissolution−recrystallization manner (see Figure 2B−D).[47] Figure 2B,C displays the intermediate states of this morphological evolution with increasing reaction time, in which the transformation of pinecone-like δ-MnO_2 aggregate to needlelike α-MnO_2 nanowire is easily observed. Combined with the above XRD results, the stepwise process of MnO_2 morphological evolution and phase transition is therefore proposed and shown in Figure 3. The morphology and phase transition occurred simultaneously during the hydrothermal reaction process. It is worth noting that the amorphous to δ and further to α phase transition is the main pathway for the formation of α-MnO_2, of which the amorphous-to-δ phase transition is likely to be the kinetic-controlled step of the stepwise transition chain.[45] Besides, N_2 physisorption results in Figure S2 and Table S2 (Supporting Information) indicate that the BET specific surface areas are 209, 61, 206, and 88 $m^2\ g^{-1}$ for MnO_2-1h, MnO_2-2h, MnO_2-5h, and MnO_2-12h, respectively, which is in good agreement with the morphological results (Figure 2).

Figure 4A shows the survey XPS spectrum of MnO_2-1h. The typical peaks in the spectrum can be assigned to C 1s, O 1s, Mn 3s, Mn 2p, and K 2p respectively, confirming the presence of C, O, Mn, and K elements. Note that the C 1s peak at approximately 284.6 eV is attributed to the adventitious carbon from the atmosphere. The K 2p peak is derived from one of the manganese sources (i.e., $KMnO_4$), of which potassium is the initially intercalated cation of the layered MnO_2 matrix.[48] The O 1s peaks at 529.7, 530.4, and 531.5 eV are due to the tetravalent oxide (Mn−O−−Mn), hydrated trivalent oxide (Mn−O−H), and the residual water molecule (H−O−H), respectively (Figure 4B). The Mn 2p spectrum in Figure 4C exhibits two peaks at 642.4 and 654.0 eV with a spin-energy separation of 11.6 eV, which is in good agreement with the binding energies of Mn $2p_{3/2}$ and Mn $2p_{1/2}$, respectively, suggesting that Mn element mainly exists as a chemical state of Mn^{4+}.[22] Also, a spin-energy separation of 4.8 eV was also observed in the Mn 3s spectrum (Figure 4D), further confirming the presence of Mn^{4+}.[49] In terms of the similarity in the synthetic procedure of all MnO_2 samples and the above XRD results, it is, therefore, believed that the manganese valence in other MnO_2 samples (i.e., MnO_2-2h, MnO_2-5h, and MnO_2-12h) is also +4.

Electrochemical Tests of MnO_2 Electrodes. CV curves of MnO_2 electrodes obtained in a 1 M NaCl solution at various scanning rates are shown in Figure S3 (Supporting Information). The leaflike-shaped voltammograms of MnO_2-1h, MnO_2-2h, and MnO_2-5h, especially at high scanning rates (i.e., 50 and 100 mV s^{-1}), indicated less ideal capacitive behaviors of such MnO_2 electrodes as compared to the MnO_2-12h electrode with a rectangular-shaped voltammogram in the potential window of 0−0.8 V. This observation is in good agreement with early reports on manganese-based electrodes, exhibiting a typical pseudocapacitive behavior.[23,35,36] Figure 5A depicts the CV curves of MnO_2 electrodes at a scanning rate of 5 mV s^{-1}. Curves of MnO_2-1h, MnO_2-2h, and MnO_2-5h are distorted with redox peaks, which are attributed to the Faradaic reactions of redox-active MnO_2.[23,50] Of these samples, MnO_2-1h exhibits the largest area under the curve, indicating that it has the highest specific capacitance (also see Figure 5C) and thus the best electrosorption performance.

Figure 5B presents the GCD curves of MnO_2 electrodes tested in 1 M NaCl solution at a current density of 0.3 A g^{-1}. The curves exhibit an essential linear voltage/time relationship with minor curvatures near 0 V, which is rational because the deviation of the linear GCD curve is a sign of pseudocapacitive behavior of MnO_2 electrodes.[23] Note that MnO_2-1h has a considerably longer discharge time than those of other MnO_2 electrodes, implying a higher ion storage feature of MnO_2-1h than the other MnO_2 electrodes,[51] which is in good accordance with the above CV results. The specific capacitance (C, F g^{-1}) can be calculated from the discharge curve using eq 5,

$$C = \frac{I\ \Delta t}{m\ \Delta V} \tag{5}$$

where I is the discharge current (A), Δt is the discharge time (s), m is the mass of active material (g), and ΔV is the voltage change (V) excluding IR (current resistance) drop in the discharge process. GCD curves of MnO_2 electrodes in 1 M NaCl at various specific currents (0.3−2 A g^{-1}) are also given in Figure S4 (Supporting Information). All GCD curves are featured by a nearly triangular and symmetric shape, indicating high reversibility of these MnO_2 electrodes. It is worth noting that the symmetry of triangular-like GCD curves is likely to be improved orderly (Figure 5B), and the charge−discharge time decreases clearly as the δ-to-α phase transition proceeds (i.e., MnO_2-1h → MnO_2-12h), indicating better reversibility but a smaller specific capacitance of highly crystalline α-MnO_2 than poorly crystalline δ-MnO_2. This observation further confirms the above CV results and has also been reported elsewhere.[22,23] The IR drops were measured according to the discharge curves at different specific currents. As shown in Figures S4 and S5 (Supporting Information), the IR drops on all of the curves were similar and small. For the MnO_2-1h electrode, the smallest IR drops of 9, 11, 14, 28, and 55 mV were obtained at 0.3, 0.4, 0.5, 1, and 2 A g^{-1}, respectively, indicating that the MnO_2-1h electrode has the lowest internal charge-transfer resistances (Table S3, Supporting Information) and excellent capacitive properties.

Figure 5C shows the specific capacitances of the MnO_2 electrodes derived from the GCD curves (Figure S4, Supporting Information) as a function of specific current. A specific capacitance as high as 203.9 F g^{-1} was obtained for the MnO_2-1h electrode at a specific current of 0.3 A g^{-1}, which is about 1.7 times that for the MnO_2-12 electrode at the same conditions (Table S2, Supporting Information). This observation is in good agreement with early reports.[23,52] Figure 5D shows EIS data and the Nyquist plots of MnO_2 electrodes. The equivalent electric circuit used to fit the Nyquist plots is also given as the inset. The EIS curves consist of semicircles in the high-frequency region and nearly straight lines in the low-frequency region. Generally, the diameter of semicircle refers to the charge-transfer resistance (R_{ct}), which is attributed to the redox reaction at the electrode/electrolyte interface. The fitting R_{ct} values of MnO_2-1h, MnO_2-2h, MnO_2-5h, and MnO_2-12h are 2.86, 3.41, 3.54, and 3.23 Ω, respectively. Thus, it is reasonable to expect that MnO_2-1h with the lowest R_{ct} has the best charge-transfer performance in the electrolyte solution. The slope of the straight lines that followed the semicircles is Warburg impedance (Z_w), which is attributed to the interfacial ion migration from the electrolyte to the electrode. Note that the slope values follow the order MnO_2-12h ≈ MnO_2-5h < MnO_2-2h < MnO_2-1h electrode (Figure 5D), confirming that needlelike α-MnO_2 has a higher ion migration rate than that of

https://dx.doi.org/10.1021/acssuschemeng.0c04101
ACS Sustainable Chem. Eng. 2020, 8, 11424−11434

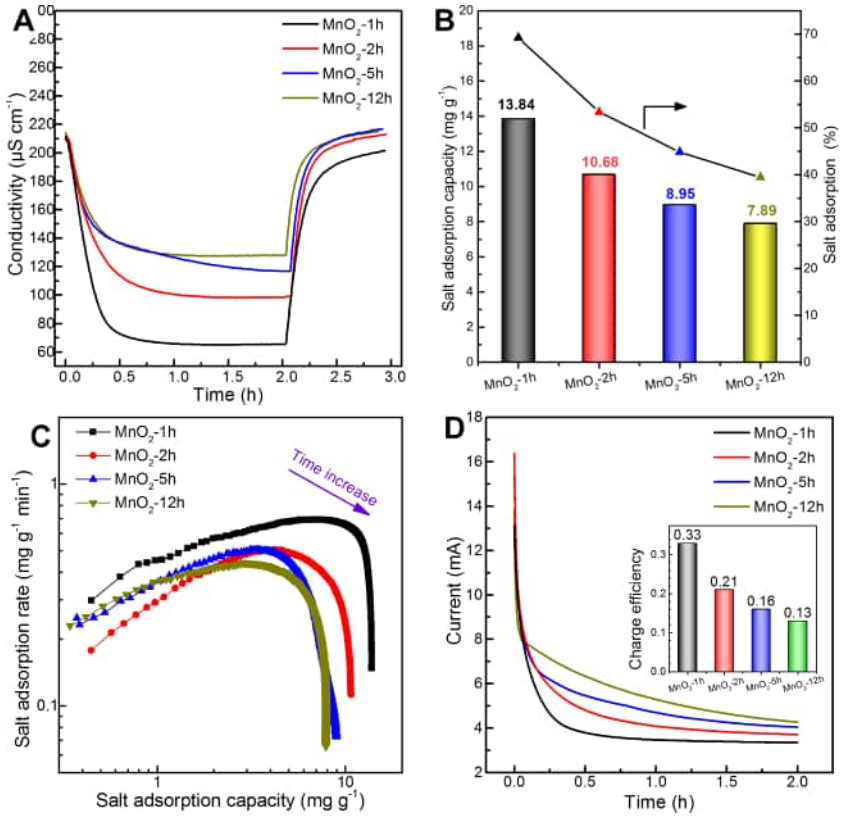

Figure 6. (A) CDI performance of MnO_2 electrodes, (B) salt adsorption capacity and the salt adsorption percentage of MnO_2 electrodes in 100 mg L^{-1} NaCl (1.71 mM), (C) Kim–Yoon plots of MnO_2 electrodes, and (D) current responses of MnO_2 electrodes.

Table 1. Comparison of Salt Adsorption Performance Reported for MnO_2-Based Electrodes Applied for CDI

electrodes[a]	feedwater salt concentration (mg L^{-1})	working potential (V)	cell mode	salt adsorption capacity (mg g^{-1})	ref
AC@α-MnO_2	584.4	1.0	CDI	9.3	22
PCS@δ-MnO_2	40	1.8	CDI	6.28	31
MWCNTs@δ-MnO_2	87	1.8	CDI	6.65	32
VACNT@MnO_x	100	1.2	CDI	28.6	35
OMC@MnO_x	40	1.2	CDI	5.4	33
graphene@α-MnO_2	70	1.2	CDI	5.01	24
RGO@Mn_3O_4	1000	1.2	CDI	34.2	36
ECNF@MnO_x	500	1.2	CDI	8.2	34
HC@δ-MnO_2	100	1.2	HCDI	19.6	28
α-MnO_2	1170	1.0	HCDI	9.93	23
α-MnO_2 NWs	876.6	1.2	HCDI[c]	22.1	8
Mn_3O_4 NWs	1000	1.2	CDI	23.7	36
δ-MnO_2[b]	500	1.4	HCDI	14.9	7
MnO_2-1h	100	1.2	HCDI	13.84	this study
MnO_2-1h	200	1.2	HCDI	16.14	this study
MnO_2-1h	500	1.2	HCDI	21.32	this study

[a]Note: AC, activated carbon; PCS, porous carbon sphere; MWCNTs, multiwalled carbon nanotubes; VACNT, vertically aligned carbon nanotubes; OMC, ordered mesoporous carbon; RGO, reduced graphene oxide; ECNF, electrospun carbon nanofiber; HC, hollow carbon; NWs, nanowires. [b]MnO_2 was used as the anode in the HCDI cell. [c]With anion- and cation-exchange membranes.

poorly crystalline δ-MnO_2.[43] Moreover, the equivalent series resistance (R_s) was obtained from the intercept of the semicircle at the real axis (Z') and can be used to assess the electrical conductivity of the electrodes. The MnO_2-1h electrode displays a smaller R_s than those of other MnO_2 electrodes, suggesting that the MnO_2-1h electrode has a higher electrical conductivity than other crystalline MnO_2 electrodes. It has been reported that both the morphological feature and the phase composition play a crucial role in governing the above EIS parameters.[43] As shown in Figures 2 and 5D, it appears that R_s values follow the order needlelike α-MnO_2 nanowires (MnO_2-12h) < poorly crystalline δ-MnO_2 (MnO_2-1h) < pinecone-like crystalline δ-MnO_2 (MnO_2-2h) < mixture of pinecone-like crystalline δ-MnO_2 and needlelike α-MnO_2 nanowires (MnO_2-5h) (Table S3, Supporting Information). This observation is in good agreement with a previous report that the higher the crystallinity of the MnO_2 electrode, the greater the corresponding equivalent series resistance.[23]

https://dx.doi.org/10.1021/acssuschemeng.0c04101
ACS Sustainable Chem. Eng. 2020, 8, 11424–11434

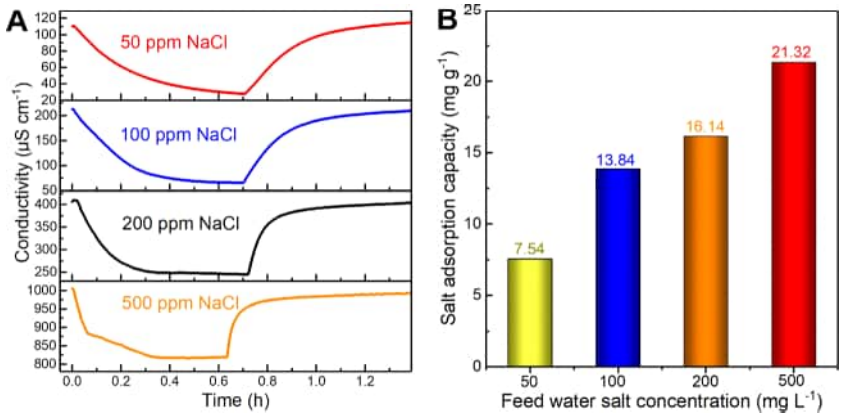

Figure 7. (A) CDI performances of MnO_2-1h in NaCl solution with varying concentrations and (B) salt adsorption capacities of the MnO_2-1h electrode as a function of the feedwater salt concentrations.

Performance of Capacitive Deionization. The desalination performance of MnO_2 electrodes was investigated through batch mode membrane-free HCDI experiments under a cell voltage of 1.2 V. Figure 6A shows the electrosorption/desorption curves of these MnO_2 electrodes in 100 mg L^{-1} NaCl (1.71 mM) solution.

All curves are featured by the characteristic three stages—the electrosorption stage, the saturation stage, and the desorption stage. It is apparent that the poorly crystalline MnO_2 electrode (i.e., MnO_2-1h) underwent a more rapid decrease in solution conductivity than the crystalline MnO_2 (e.g., MnO_2-5h, and MnO_2-12h). This observation is consistent with the earlier data elsewhere.[23] The SACs calculated by eq 1 and the corresponding salt removal percentages are shown in Figure 6B. Among all MnO_2 electrodes, MnO_2-1h exhibits the highest SAC (13.84 mg g^{-1}) and the greatest deionization percentage (69.2%) in 100 mg L^{-1} NaCl (1.71 mM) solution. The SACs in 100 mg L^{-1} NaCl (1.71 mM) solution are 10.68, 8.95, and 7.89 mg g^{-1} for MnO_2-2h, MnO_2-5h, and MnO_2-12h electrodes, respectively. Note that the BET specific surface areas of MnO_2 samples follow the order MnO_2-1h > MnO_2-5h > MnO_2-12h > MnO_2-2h (Table S2, Supporting Information). It is no doubt that a higher surface area can offer more sites for ion adsorption when the dominant salt uptake mechanism is surface adsorption. Therefore, Leong et al. attributed the higher salt adsorption of poorly crystalline MnO_2 to its high surface area.[23] If this is true, considering that both MnO_2-1h and MnO_2-2h exhibited very similar crystal structures (Table 1) and that MnO_2-1h has a BET surface area (209 m^2 g^{-1}, Table S2) 3.4 times that of MnO_2-2h (61 m^2 g^{-1}), the SAC of MnO_2-1h electrode should be about 2.4 times greater than that of the MnO_2-2h electrode. However, as shown in Table S2, the SAC value of the MnO_2-1h electrode is only about 1.3 times that of the MnO_2-2h electrode, suggesting that salt adsorption was not governed by surface adsorption. To elucidate the underlying ion adsorption mechanism, we have determined the Na/Mn atomic ratio of the cycled MnO_2 electrodes after the removal of all of the surface-adsorbed ions by excess pure water, and the results are shown in Table S4 (Supporting Information). Note that the Na/Mn ratio follows the order MnO_2-12h < MnO_2-5h < MnO_2-2h < MnO_2-1h and that all of the fractions of ion intercalation to the total ion removal capacity are much greater than 50%, implying that the bulk ion intercalation reaction is the dominant mechanism of ion removal for all MnO_2 electrodes. It is believed that the lower the crystallinity of δ-MnO_2, the looser the layers of edge-sharing MnO_6 octahedra and thus the more the interlayer spaces for Na^+ ion storage.[52] Therefore, the higher specific capacitance and thus the higher SAC of MnO_2-1h compared to that of MnO_2-2h could be attributed to its lower crystallinity. Furthermore, the 2D layered structure with a tunnel width of ~ 7.24 Å (d_{001}) of δ-MnO_2 can facilitate the diffusion of Na^+ ions (the radius of hydrated Na^+, r_s = 3.6 Å)[52] in and out of the interlayer region, resulting in fast ion transport with a low diffusion limit. In contrast, 1D α-MnO_2 nanowires with tunnel sizes of 1 × 1 (1.89 Å) and 2 × 2 (4.6 Å) will prefer to trap less solvated Na^+ ions into the tunnels, leading to slow ion transport.[8,23,38,53] Note that α-MnO_2 nanowires exhibit less specific capacitance when compared to other nanostructures including α-MnO_2 nanosheets, nanospheres, and nanotubes.[52] It is, therefore, reasonable to attribute the best desalination performance of MnO_2-1h to its lowest crystallinity and hence the highest crystallographic volumes derived from the 2D interlayer channels (7.24 Å) for Na^+ storage in the layered structure of poorly crystalline δ-MnO_2. Besides, a higher BET surface area and a larger total pore volume will facilitate the diffusion of Na^+ ions into the interlayer region.[23,52]

Figure 6C displays the Kim–Yoon plot of these MnO_2 electrodes. In general, the more the SAR vs SAC profiles approaching to the top-right corner of the Kim–Yoon plot, the better the performance in both SAR and SAC of the electrodes that can be expected.[42] The distance between the SAR vs SAC profiles and the top-right corner follows the order MnO_2-1h < MnO_2-2h < MnO_2-5h < MnO_2-12h, suggesting that the MnO_2-1h electrode can trap ions at the most rapid rate. Figure 6D presents the current response of these MnO_2 electrodes in 100 mg L^{-1} NaCl (1.71 mM) solution. The Λ values calculated using eq 2 are approximately 0.33, 0.21, 0.16, and 0.13 for MnO_2-1h, MnO_2-2h, MnO_2-5h, and MnO_2-12h, respectively. Note that the poorly crystalline MnO_2 electrode (i.e., MnO_2-1h) has the highest charge efficiency, further confirming that the MnO_2-1h electrode exhibits the best desalination performance among all of the MnO_2 electrodes. Therefore, the MnO_2-1h electrode was chosen for further desalination testing.

We further tested the MnO_2-1h electrode in salt solutions of varying concentrations from 50 to 500 mg L^{-1} (0.86–8.56 mM), and the results are shown in Figure 7. Obviously, the greater the salt concentrations, the sooner the electrosorption

https://dx.doi.org/10.1021/acssuschemeng.0c04101
ACS Sustainable Chem. Eng. 2020, 8, 11424–11434

reaching an equilibrium state under the same conditions (Figure 7A). The salt concentration difference (gradient) across the interface of MnO_2 electrodes also contributes to the electrosorption rate besides the electric field gradient of HCDI cells. It is, therefore, undoubted that a higher salt concentration in the feed solution will lead to a greater driving force facilitating salt diffusion from the bulk solution to the inner pores of the electrodes and hence a shorter period to reach equilibrium. Note that SAC of the poorly crystalline MnO_2-1h electrode is approximately proportional to the salt concentrations of the feed solutions (Figure 7B), which was also observed for MnO_2 electrodes by other investigators.[23,28] The SACs of the MnO_2-1h electrode in 100 mg L^{-1} (1.71 mM), 200 mg L^{-1} (3.42 mM), and 500 mg L^{-1} (8.56 mM) NaCl solutions are 13.84, 16.14, and 21.32 mg g^{-1}, respectively, suggesting that our poorly crystalline MnO_2-1h is among the top three best MnO_2 electrodes as compared to other MnO_2-based electrodes (Figure S6 and Table 1).

Recycling Performance. The recycling performance of the MnO_2-1h electrode was first evaluated in 100 mg L^{-1} NaCl (1.71 mM) solution for five desalination cycles, as shown in Figure S7A. Both the charge−discharge process and the corresponding response current exhibit similar periodical patterns with time (Figure S7B,C, Supporting Information), indicative of the electrosorption−desorption of ions in HCDI cells.[22] A slight decrease in SAC was observed for the MnO_2-1h electrode after the fifth cycle (Figure S7A, Supporting Information). The SAC of MnO_2-1h is 11.61 mg g^{-1} after five cycles (inset of Figure S7A), reserving only 83.9% of the initial SAC (i.e., 13.84 mg g^{-1}). We initially speculated that the decrease in desalination capacity is derived from the possible structural degradation in the MnO_2 electrode[23,53] because the initial intercalated K^+ ions of the MnO_2-1h electrode (Figure 4A) were detected by ICP-OES in the cell solution after 20 cycles (data not shown), indicating that K^+ ions were gradually replaced by Na^+.[7] The highly frequent intercalation reactions between Na^+ and K^+ will probably disorder the poorly crystalline MnO_2-1h and hence decrease the cycling performance of the MnO_2-1h electrode. However, solid evidence provided by the XRD pattern of the MnO_2-1h electrode after 20 desalination cycles (Figure S8, Supporting Information) indicates that no phase transition occurred during the desalination process. Further experimental evidence from ICP-OES measurements of the cell solution (data not shown) suggests that the loss of Mn element from the cathode to the bulk solution is only about 1.7% in the 20th cycle. All of the above data indicate that the MnO_2-1h cathode is stable and rigid enough during the recycling evaluation.

The second attempt of a recycling experiment focusing on the stability of the AC anode of the HCDI cell was carried out in 100 mg L^{-1} NaCl (1.71 mM) solution for 68 cycles (Figure S7C, Supporting Information). Apparently, in the first 24 cycles with the use of the original MnO_2-1h cathode and AC anode, the SAC decreased from 13.43 mg g^{-1} for the first run to 5.33 mg g^{-1} for the 24th run. After renewing the used AC anode with a new one for the first time, the SAC has recovered to 12.92 mg g^{-1} (the 25th run) and then gradually decreased to 8.18 mg g^{-1} after 46 desalination cycles. A second renewing the AC anode from the 47th run also recovered the desalination capacity to 13.72 mg g^{-1} (the 47th run) and then remained to 8.07 mg g^{-1} for the 68th run. Therefore, the decrease in desalination capacity of the MnO_2-1h electrode is attributed mainly to the degradation of the AC anode rather than the MnO_2-1h cathode during the desalination recycling test.

CONCLUSIONS

In this work, MnO_2 materials with tailorable phase compositions and crystallinity were synthesized and then evaluated as electrodes in a membrane-free HCDI cell. The effects of phase composition and crystallinity of MnO_2 electrode materials on the desalination efficiency were considered for the first time. The poorly crystalline 2D lamellar-structured δ-MnO_2 with a lot of amorphous phases (MnO_2-1h), rather than the highly crystalline 1D α-MnO_2 nanowire (MnO_2-12h), demonstrated the highest salt adsorption capacity and the largest charge efficiency. Combined results of the MnO_2 crystallinities, SACs, Na/Mn atomic ratios, and the Na^+ fractions of both surface adsorption and bulk ion intercalation revealed that ion removal from the solution was because of the bulk ion intercalation for both poorly and highly crystalline MnO_2 electrodes. Our data of chemical and phase compositions of the cycled MnO_2-1h electrode indicated that the decrease in SACs during the recycling test was derived in part from the exfoliation and dissolution of the MnO_2 electrode. These findings emphasize the importance of both the phase composition and the crystallinity of MnO_2 electrodes in defining the desalination performance and the need for further investigation to improve the SAC and the structural stability of poorly crystalline MnO_2 materials used in HCDI for water desalination.

ASSOCIATED CONTENT

Supporting Information

The Supporting Information is available free of charge at https://pubs.acs.org/doi/10.1021/acssuschemeng.0c04101.

Phase weight percentages of MnO_2; pore, microstructure, and electrochemical characterization data of MnO_2; Na^+ fractions in cycled electrodes; schematic of the CDI device; N_2 absorption−desorption isotherms and pore size distribution of MnO_2; curves of CV, GCD, and IR drops of electrodes; comparison of the maximum SACs of electrodes with previous references; curves of recycling performance and the corresponding current response of the MnO_2-1h electrode; and XRD patterns of the MnO_2-1h electrode before and after desalination (PDF)

AUTHOR INFORMATION

Corresponding Authors

Yang Li − *Collaborative Innovation Center of Atmospheric Environment and Equipment Technology, Jiangsu Key Laboratory of Atmospheric Environment Monitoring and Pollution Control, School of Environmental Science and Engineering, Nanjing University of Information Science and Technology, Nanjing 210044, China*; Email: lysn6381@nuist.edu.cn

Feihu Li − *Collaborative Innovation Center of Atmospheric Environment and Equipment Technology, Jiangsu Key Laboratory of Atmospheric Environment Monitoring and Pollution Control, School of Environmental Science and Engineering, Nanjing University of Information Science and Technology, Nanjing 210044, China*; orcid.org/0000-0002-2969-8276; Email: fhli@nuist.edu.cn

https://dx.doi.org/10.1021/acssuschemeng.0c04101
ACS Sustainable Chem. Eng. 2020, 8, 11424−11434

Authors

Jie Jin − *Collaborative Innovation Center of Atmospheric Environment and Equipment Technology, Jiangsu Key Laboratory of Atmospheric Environment Monitoring and Pollution Control, School of Environmental Science and Engineering, Nanjing University of Information Science and Technology, Nanjing 210044, China*

Man Li − *Collaborative Innovation Center of Atmospheric Environment and Equipment Technology, Jiangsu Key Laboratory of Atmospheric Environment Monitoring and Pollution Control, School of Environmental Science and Engineering, Nanjing University of Information Science and Technology, Nanjing 210044, China*

Mengting Tang − *School of Chemistry and Materials Science, Nanjing University of Information Science and Technology, Nanjing 210044, China*

Yangyang Liu − *Collaborative Innovation Center of Atmospheric Environment and Equipment Technology, Jiangsu Key Laboratory of Atmospheric Environment Monitoring and Pollution Control, School of Environmental Science and Engineering, Nanjing University of Information Science and Technology, Nanjing 210044, China*

Hui Cao − *School of Chemistry and Materials Science, Nanjing University of Information Science and Technology, Nanjing 210044, China;* orcid.org/0000-0002-6797-2627

Complete contact information is available at: https://pubs.acs.org/10.1021/acssuschemeng.0c04101

Author Contributions

F.L. designed the research; F.L., J.J., M.L., M. T., Y.Li, Y.Liu, and H.C. performed the research; F.L., J.J., and Y.Li analyzed the data; and F.L. and J.J. wrote the paper.

Notes

The authors declare no competing financial interest.

■ ACKNOWLEDGMENTS

The work was financially supported by the Innovation Program for Postgraduate Research of Jiangsu Province (SJKY19-0977), NSFC (51002080, 41501197), SPITP (201810300041Z), the Top-notch Academic Programs Project of Jiangsu Higher Education Institutions (PPZY2015C222), and the Priority Academic Program Development (PAPD) of Jiangsu Higher Education Institutions.

■ REFERENCES

(1) Eliasson, J. The rising pressure of global water shortages. *Nature* **2015**, *517*, 6.

(2) Greenlee, L. F.; Lawler, D. F.; Freeman, B. D.; Marrot, B.; Moulin, P. Reverse osmosis desalination: Water sources, technology, and today's challenges. *Water Res.* **2009**, *43*, 2317−2348.

(3) Subramani, A.; Jacangelo, J. G. Emerging desalination technologies for water treatment: A critical review. *Water Res.* **2015**, *75*, 164−187.

(4) Porada, S.; Zhao, R.; van der Wal, A.; Presser, V.; Biesheuvel, P. M. Review on the science and technology of water desalination by capacitive deionization. *Prog. Mater. Sci.* **2013**, *58*, 1388−1442.

(5) Oren, Y. Capacitive delonization (CDI) for desalination and water treatment - past, present and future (a review). *Desalination* **2008**, *228*, 10−29.

(6) Suss, M. E.; Porada, S.; Sun, X.; Biesheuvel, P. M.; Yoon, J.; Presser, V. Water desalination via capacitive deionization: what is it and what can we expect from it? *Energy Environ. Sci.* **2015**, *8*, 2296−2319.

(7) Wu, T. T.; Wang, G.; Wang, S. Y.; Zhan, F.; Fu, Y.; Qiao, H. Y.; Qiu, J. S. Highly Stable Hybrid Capacitive Deionization with a MnO2 Anode and a Positively Charged Cathode. *Environ. Sci. Technol. Lett.* **2018**, *5*, 98−102.

(8) Byles, B. W.; Cullen, D. A.; More, K. L.; Pomerantseva, E. Tunnel structured manganese oxide nanowires as redox active electrodes for hybrid capacitive deionization. *Nano Energy* **2018**, *44*, 476−488.

(9) Li, Z.; Song, B.; Wu, Z. K.; Lin, Z. Y.; Yao, Y. G.; Moon, K. S.; Wong, C. P. 3D porous graphene with ultrahigh surface area for microscale capacitive deionization. *Nano Energy* **2015**, *11*, 711−718.

(10) Liu, Y.; Nie, C. Y.; Liu, X. J.; Xu, X. T.; Sun, Z.; Pan, L. K. Review on carbon-based composite materials for capacitive deionization. *RSC Adv.* **2015**, *5*, 15205−15225.

(11) Han, B.; Cheng, G.; Wang, Y. K.; Wang, X. K. Structure and functionality design of novel carbon and faradaic electrode materials for high-performance capacitive deionization. *Chem. Eng. J.* **2019**, *360*, 364−384.

(12) Wang, G.; Dong, Q.; Ling, Z.; Pan, C.; Yu, C.; Qiu, J. S. Hierarchical activated carbon nanofiber webs with tuned structure fabricated by electrospinning for capacitive deionization. *J. Mater. Chem.* **2012**, *22*, 21819−21823.

(13) Hou, C. H.; Huang, C. Y. A comparative study of electrosorption selectivity of ions by activated carbon electrodes in capacitive deionization. *Desalination* **2013**, *314*, 124−129.

(14) Jia, B. P.; Zou, L. D. Wettability and its influence on graphene nansoheets as electrode material for capacitive deionization. *Chem. Phys. Lett.* **2012**, *548*, 23−28.

(15) Zhang, D. S.; Yan, T. T.; Shi, L. Y.; Peng, Z.; Wen, X. R.; Zhang, J. P. Enhanced capacitive deionization performance of graphene/carbon nanotube composites. *J. Mater. Chem.* **2012**, *22*, 14696−14704.

(16) Dutta, S.; Huang, S. Y.; Chen, C.; Chen, J. E.; Alothman, Z. A.; Yamauchi, Y.; Hou, C. H.; Wu, K. C. W. Cellulose Framework Directed Construction of Hierarchically Porous Carbons Offering High-Performance Capacitive Deionization of Brackish Water. *ACS Sustainable Chem. Eng.* **2016**, *4*, 1885−1893.

(17) Huang, Z. H.; Yang, Z. Y.; Kang, F. Y.; Inagaki, M. Carbon electrodes for capacitive deionization. *J. Mater. Chem. A* **2017**, *5*, 470−496.

(18) Porada, S.; Weinstein, L.; Dash, R.; van der Wal, A.; Bryjak, M.; Gogotsi, Y.; Biesheuvel, P. M. Water Desalination Using Capacitive Deionization with Microporous Carbon Electrodes. *ACS Appl. Mater. Interfaces* **2012**, *4*, 1194−1199.

(19) La Mantia, F.; Pasta, M.; Deshazer, H. D.; Logan, B. E.; Cui, Y. Batteries for Efficient Energy Extraction from a Water Salinity Difference. *Nano Lett.* **2011**, *11*, 1810−1813.

(20) Lee, J.; Kim, S.; Kim, C.; Yoon, J. Hybrid capacitive deionization to enhance the desalination performance of capacitive techniques. *Energy Environ. Sci.* **2014**, *7*, 3683−3689.

(21) Wei, W.; Cui, X.; Chen, W. X.; Ivey, D. G. Manganese oxide-based materials as electrochemical supercapacitor electrodes. *Chem. Soc. Rev.* **2011**, *40*, 1697−1721.

(22) Liu, Y. H.; Hsi, H. C.; Li, K. C.; Hou, C. H. Electrodeposited Manganese Dioxide/Activated Carbon Composite As a High-Performance Electrode Material for Capacitive Deionization. *ACS Sustainable Chem. Eng.* **2016**, *4*, 4762−4770.

(23) Leong, Z. Y.; Yang, H. Y. A Study of MnO2 with Different Crystalline Forms for Pseudocapacitive Desalination. *ACS Appl. Mater. Interfaces* **2019**, *11*, 13176−13184.

(24) El-Deen, A. G.; Barakat, N. A. M.; Kim, H. Y. Graphene wrapped MnO2-nanostructures as effective and stable electrode materials for capacitive deionization desalination technology. *Desalination* **2014**, *344*, 289−298.

(25) Hand, S.; Cusick, R. D. Characterizing the Impacts of Deposition Techniques on the Performance of MnO2 Cathodes for Sodium Electrosorption in Hybrid Capacitive Deionization. *Environ. Sci. Technol.* **2017**, *51*, 12027−12034.

(26) Agartan, L.; Hayes-Oberst, B.; Byles, B. W.; Akuzum, B.; Pomerantseva, E.; Kumbur, E. C. Influence of operating conditions and cathode parameters on desalination performance of hybrid CDI systems. *Desalination* **2019**, *452*, 1−8.
(27) Wang, S. Y.; Wang, G.; Che, X. P.; Wang, S. F.; Li, C. X.; Li, D. Z.; Zhang, Y. Q.; Dong, Q.; Qiu, J. S. Enhancing the capacitive deionization performance of NaMnO2 by interface engineering and redox-reaction. *Environ. Sci. Nano* **2019**, *6*, 2379−2388.
(28) Wang, S..; Wang, G.; Wu, T.; Li, C.; Wang, Y.; Pan, X.; Zhan, F.; Zhang, Y.; Wang, S.; Qiu, J. Membrane-Free Hybrid Capacitive Deionization System Based on Redox Reaction for High-Efficiency NaCl Removal. *Environ. Sci. Technol.* **2019**, *53*, 6292−6301.
(29) Tang, K. X.; Hong, T. Z. X.; You, L. M.; Zhou, K. Carbon−metal compound composite electrodes for capacitive deionization: synthesis, development and applications. *J. Mater. Chem. A* **2019**, *7*, 26693−26743.
(30) Yang, J.; Zou, L. D.; Song, H. H.; Hao, Z. P. Development of novel MnO2/nanoporous carbon composite electrodes in capacitive deionization technology. *Desalination* **2011**, *276*, 199−206.
(31) Chen, B. W.; Wang, Y. F.; Yu, F.; Zhu, Y. S.; Zhang, L. X.; Wu, Y. P. Enhanced Capacitive Desalination Performance of Porous Carbon Spheres@MnO2 Composite. *Chin. J. Chem.* **2017**, *35*, 55−60.
(32) Chen, B. W.; Wang, Y. F.; Chang, Z.; Wang, X. W.; Li, M. X.; Liu, X.; Zhang, L. X.; Wu, Y. P. Enhanced capacitive desalination of MnO2 by forming composite with multi-walled carbon nanotubes. *RSC Adv.* **2016**, *6*, 6730−6736.
(33) Zhao, C. X.; Lv, X. Y.; Li, J. S.; Xie, T.; Qi, Y. Y.; Chen, W. Manganese Oxide Nanoparticles Decorated Ordered Mesoporous Carbon Electrode for Capacitive Deionization of Brackish Water. *J. Electrochem. Soc.* **2017**, *164*, E505−E511.
(34) Cai, W. S.; Xiong, Z. B.; Hussain, T.; Yang, J. M.; Wang, Y. B.; Liu, J. Porous MnOx Covered Electrospun Carbon Nanofiber for Capacitive Deionization. *J. Electrochem. Soc.* **2016**, *163*, A2515−A2523.
(35) Shi, W. B.; Zhou, X. C.; Li, J. Y.; Meshot, E. R.; Taylor, A. D.; Hu, S.; Kim, J. H.; Elimelech, M.; Plata, D. L. High-Performance Capacitive Deionization via Manganese Oxide-Coated, Vertically Aligned Carbon Nanotubes. *Environ. Sci. Technol. Lett.* **2018**, *5*, 692−700.
(36) Bharath, G.; Arora, N.; Hai, A.; Banat, F.; Savariraj, D.; Taher, H.; Mangalaraja, R. V. Synthesis of hierarchical Mn3O4 nanowires on reduced graphene oxide nanoarchitecture as effective pseudocapacitive electrodes for capacitive desalination application. *Electrochim. Acta* **2020**, *337*, No. 135668.
(37) De Guzman, R. N.; Awaluddin, A.; Shen, Y. F.; Tian, Z. R.; Suib, S. L.; Ching, S.; O'Young, C. L. Electrical Resistivity Measurements on Manganese Oxides with Layer and Tunnel Structures: Birnessites, Todorokites, and Cryptomelanes. *Chem. Mater.* **1995**, *7*, 1286−1292.
(38) Yuan, Y. F.; Liu, C.; Byles, B. W.; Yao, W. T.; Song, B. A.; Cheng, M.; Huang, Z. N.; Amine, K.; Pomerantseva, E.; Shahbazian-Yassar, R.; Lu, J. Ordering Heterogeneity of [MnO6] Octahedra in Tunnel-Structured MnO2 and Its Influence on Ion Storage. *Joule* **2019**, *3*, 471−484.
(39) Xu, S.; Wang, T. H.; Wang, C. F.; Chen, C. W.; Dong, C. D.; Huang, C. P. The effect of crystal phase of manganese oxide on the capacitive deionization of simple electrolytes. *Sci. Total Environ.* **2019**, *675*, 31−40.
(40) Ragupathy, P.; Vasan, H. N.; Munichandraiah, N. Synthesis and characterization of nano-MnO2 for electrochemical supercapacitor studies. *J. Electrochem. Soc.* **2008**, *155*, A34−A40.
(41) Stoller, M. D.; Ruoff, R. S. Best practice methods for determining an electrode material's performance for ultracapacitors. *Energy Environ. Sci.* **2010**, *3*, 1294−1301.
(42) Kim, T.; Yoon, J. CDI ragone plot as a functional tool to evaluate desalination performance in capacitive deionization. *RSC Adv.* **2015**, *5*, 1456−1461.
(43) Bai, X. L.; Tong, X. L.; Gao, Y. L.; Zhu, W. Q.; Fu, C.; Ma, J. Y.; Tan, T. C.; Wang, C. L.; Luo, Y. S.; Sun, H. B. Hierarchical multidimensional MnO2 via hydrothermal synthesis for high performance supercapacitors. *Electrochim. Acta* **2018**, *281*, 525−533.
(44) Julien, C. M.; Massot, M.; Poinsignon, C. Lattice vibrations of manganese oxides. Part I. Periodic structures. *Spectrochim. Acta, Part A* **2004**, *60*, 689−700.
(45) Li, Y. F.; Zhu, S. C.; Liu, Z. P. Reaction Network of Layer-to-Tunnel Transition of MnO2. *J. Am. Chem. Soc.* **2016**, *138*, 5371−5379.
(46) Yuan, Y. F.; He, K.; Byles, B. W.; Liu, C.; Amine, K.; Lu, J.; Pomerantseva, E.; Shahbazian-Yassar, R. Deciphering the Atomic Patterns Leading to MnO2 Polymorphism. *Chem* **2019**, *5*, 1793−1805.
(47) Fu, X.; Huo, W. C.; Liu, X. Y.; Shan, Q. Y.; Guo, Z. Y.; Jing, C.; Dong, F.; Yao, H. C.; Zhang, Y. X.; Chen, K. Morphological evolution process of delta-MnO2 from 2-D to 1-D without phase transition. *CrystEngComm* **2019**, *21*, 4593−4598.
(48) Subramanian, V.; Zhu, H. W.; Vajtai, R.; Ajayan, P. M.; Wei, B. Q. Hydrothermal synthesis and pseudocapacitance properties of MnO2 nanostructures. *J. Phys. Chem. B* **2005**, *109*, 20207−20214.
(49) Yu, N.; Yin, H.; Zhang, W.; Liu, Y.; Tang, Z. Y.; Zhu, M. Q. High-Performance Fiber-Shaped All-Solid-State Asymmetric Supercapacitors Based on Ultrathin MnO2 Nanosheet/Carbon Fiber Cathodes for Wearable Electronics. *Adv. Energy Mater.* **2016**, *6*, No. 1501458.
(50) Zhang, G. N.; Ren, L. J.; Yan, Z.; Kang, L. P.; Lei, Z. B.; Xu, H.; Shi, F.; Liu, Z. H. Mesoporous-assembled MnO2 with large specific surface area. *J. Mater. Chem. A* **2015**, *3*, 14567−14572.
(51) Zhang, Z. Q.; Zhang, H. D.; Zhang, X. Y.; Yu, D. Y.; Ji, Y.; Sun, Q. S.; Wang, Y.; Liu, X. Y. Facile synthesis of hierarchical CoMoO4@NiMoO4 core-shell nanosheet arrays on nickel foam as an advanced electrode for asymmetric supercapacitors. *J. Mater. Chem. A* **2016**, *4*, 18578−18584.
(52) Tanggarnjanavalukul, C.; Phattharasupakun, N.; Kongpatpanich, K.; Sawangphruk, M. Charge storage performances and mechanisms of MnO2 nanospheres, nanorods, nanotubes and nanosheets. *Nanoscale* **2017**, *9*, 13630−13639.
(53) Byles, B. W.; Hayes-Oberst, B.; Pomerantseva, E. Ion Removal Performance, Structural/Compositional Dynamics, and Electrochemical Stability of Layered Manganese Oxide Electrodes in Hybrid Capacitive Deionization. *ACS Appl. Mater. Interfaces* **2018**, *10*, 32313−32322.

https://dx.doi.org/10.1021/acssuschemeng.0c04101
ACS Sustainable Chem. Eng. 2020, 8, 11424−11434